

## Effect of pressure on 3D distribution of P-wave velocity and attenuation in antigorite serpentinite

Tomáš Svitek<sup>1</sup>, Václav Vavryčuk<sup>2</sup>, Tomáš Lokajíček<sup>1</sup>, Matěj Petružálek<sup>1</sup>, and Hartmut Kern<sup>3</sup>

### ABSTRACT

We have developed a detailed study on the pressure dependence of P-wave velocities and amplitudes on a spherical sample of antigorite serpentinite from Val Malenco, Northern Italy. Measurements were done at room temperature and hydrostatic pressures up to 400 MPa in a pressure vessel with oil as a pressure medium. The transducer/sample assembly allows simultaneous velocity and amplitude measurements on the spherical sample in 132 independent directions. Three significant directions of the foliated sample were selected to study changes of the directional dependence (anisotropy) of velocity, amplitude, and  $Q$ -factor with increasing pressure. Remarkable differences are observed between the changes of velocity and attenuation anisotropy as pressure is increased. Although the velocity anisotropy is quite stable through all pressure levels, the attenuation anisotropy and the  $Q$ -factor vary significantly in magnitude and orientation. The variations are probably caused by the closing of microcracks due to acting hydrostatic pressure, so the contact conditions between individual minerals consolidate and the transmitting energy is less attenuating.

### INTRODUCTION

Seismic velocity and attenuation anisotropy are important properties of many crustal and mantle rocks. The velocity anisotropy characterizes the directionally dependent propagation velocity of seismic waves, whereas attenuation anisotropy controls the directionally dependent dissipation of seismic energy. The role of velocity and attenuation anisotropy in understanding the evolution of the earth crust and upper mantle is becoming increasingly important because the measured anisotropy has a structural origin. Major

constituents of the upper and lower crusts are felsic and mafic gneisses. The alignment of phyllosilicates and amphiboles in these rocks gives rise to marked anisotropy (Kern, 1993; Barruol and Kern, 1996). Seismic anisotropy observed in upper mantle rocks (peridotite and pyroxenite) is mainly due to crystallographic preferred orientation (CPO) of olivine and pyroxene, respectively (Babuška, 1984). The CPO-based calculated velocities and anisotropy describe the intrinsic (matrix) properties of a rock, whereas the experimental velocity data describe the seismic properties of the real rock, controlled by the rock matrix and the effect of microcracks and grain boundaries. These extrinsic effects are strongly affected by pressure and temperature.

In the past few years, the minerals of the serpentine group (chrysotile, lizardite, and antigorite) have received increasing interest because they play an important role in the dynamics of subduction zones (Watanabe et al., 2007). The different types of serpentine are a result of mantle wedge hydration and represent different levels in subduction zones, according to their different stabilities at P and T conditions (Ulmer and Trommsdorff, 1995; Hacker et al., 2003a, 2003b). Antigorite is stable up to pressures of 5 GPa and temperatures of approximately 600°C (Ulmer and Trommsdorff, 1995) and antigorite-rich serpentinites are characterized by a strong CPO of antigorite (Ji et al., 2013; Shao et al., 2014; Kern et al., 2015). Compared with the numerous papers referring to modeled (Jung, 2011; Watanabe et al., 2014) and measured seismic properties ( $V_P$ ,  $V_S$ ) of antigorite serpentinites (Kern et al., 1997; Ji et al., 2013; Shao et al., 2014), the papers reporting experimental measurements of the pressure dependence of wave velocity and attenuation and their anisotropies are very rare.

Measuring and determining anisotropic attenuation and its parameters are complicated from technical as well as theoretical points of view. Klíma et al. (1962, 1964) investigate the pressure dependence of the attenuation of the P-waves in diabase and greywacke, and Jackson et al. (2002) measure the seismic wave attenuation in polycrystalline olivine. To our knowledge, the only measurements of wave

Manuscript received by the Editor 4 January 2017; revised manuscript received 13 April 2017; published online 30 May 2017.

<sup>1</sup>Institute of Geology, The Czech Academy of Sciences, Prague, Czech Republic. E-mail: svitek@gli.cas.cz; lokajicek@gli.cas.cz; petruzalek@gli.cas.cz.

<sup>2</sup>Institute of Geophysics, The Czech Academy of Sciences, Prague, Czech Republic. E-mail: vv@ig.cas.cz.

<sup>3</sup>Universität Kiel, Institut für Geowissenschaften, Kiel, Germany. E-mail: kern@min.uni-kiel.de.

© 2017 Society of Exploration Geophysicists. All rights reserved.

attenuation of antigorite serpentinite are reported by Kern et al. (1997). They measure the P- and S-wave velocities and their attenuation on a cubic sample in three fabric-related orthogonal directions at pressures up to 600 MPa and temperatures to 700°C. They find, for example, that the linear slopes of the S-wave velocities ( $V_{S1}$ ,  $V_{S2}$ ) measured in the three directions greater than 100 MPa corresponded to the linear behavior of  $V_P$  and indicated no evidence for an auxetic behavior of the  $V_P/V_S$  ratio (Poisson's ratio) for the three propagation directions. The measurements also proved the remarkable anisotropic attenuation in the serpentinite and its variation with temperature and pressure. However, the experimental setting with measurements in three single directions could not provide a complete 3D distribution of rock attenuation.

This paper presents a laboratory study of joint measurements of velocity and attenuation anisotropy of antigorite serpentinite in 3D coverage together with their pressure dependency up to 400 MPa. Because ray velocity and ray attenuation are measured in the experiment, the ray quantities are recalculated to phase quantities and then inverted for parameters of general triclinic velocity and attenuation anisotropy. The variations of the pressure-induced velocity and attenuation anisotropy are analyzed in detail in the symmetry directions of velocity and amplitude extremes that relate to the mineral fabric (foliation and lineation) and of microcrack fabric (microcrack alignment).

## THE SAMPLE AND EXPERIMENTAL SETUP

### Sample characteristics

In this paper, the sample studied is a serpentinite from Val Malenco in the Western Alps, Northern Italy. It was prepared from the same block of serpentinite (sample 987) used by Kern et al. (1997, 2015). The serpentinite is an antigorite-rich rock exhibiting pronounced foliation and lineation with relics of primary olivine minerals. The foliation is defined by preferentially oriented platy antigorite grains and the lineation by the long axes of the platy antigorite minerals and elongated magnetite aggregations. A direction normal to the foliation (FN) plane as well as a direction parallel to the lineation (LD) are generally used as a reference frame in structural geology. In this work, we have selected another significant direction that corresponds to the minimum amplitude observed at 400 MPa (AD) and we compare measured and calculated quantities in these three directions. The microstructure of the sample is characterized by a pronounced microheterogeneity (Kern et al., 1997), documented by irregularly spaced millimeter-scale banding. The bands with strong foliation are dominated by oriented platy antigorite minerals that locally wrap around the elongated lenses of olivine crystals, and the bands with weaker foliation by antigorite mixed with remnants of olivine. Grain sizes of the antigorite minerals vary generally between 10 and 100  $\mu\text{m}$ , but they can go up to 500  $\mu\text{m}$ . The volume fractions determined on three orthogonal thin sections by point counting (Kern et al., 1997) and by EBSD analysis (L. Morales, personal communication, 2016) are 75–78 vol% antigorite and 18–20 vol% olivine. Synchrotron X-ray and neutron diffraction measurements (Kern et al., 2015) revealed a strong CPO of the antigorite (001) poles normal to the foliation. Although the synchrotron X-ray and neutron diffraction revealed girdles of the (100) and (010) poles within the foliation plane, the EBSD analysis (L. Morales, personal communication, 2016) showed maxima of the (100) poles oriented parallel to lineation and those of the (010) poles normal or slightly oblique to lineation

with a tendency of a girdle formation. The antigorite fabric exhibits orthotropic symmetry. At ambient conditions, the bulk density of the serpentinite, derived from the volume and the mass of the sample cube, is 2.71  $\text{g}/\text{cm}^3$ .

### Ultrasonic measurements on the spherical sample

The equipment for the measurement of the 3D velocity and amplitude distribution on the spherical sample consists of a pressure vessel connected to a two-step pressure generator, a sample positioning unit equipped with ultrasonic piezoceramic transducers allowing measurements of the P-wave attributes on samples with a diameter of 50 mm. A device for generating ultrasonic pulses, traveltime measurement, and data acquisition was used (Lokajčec and Svitek, 2015). The sample was exposed to hydrostatic pressures ranging from 0.1 to 400 MPa. The transformer oil served as the hydraulic medium. The thin layer of epoxy resin was applied as a protection against oil penetration into the sample. The acoustic signals were excited and recorded by a piezoceramic sensor pair with a resonant frequency of 2 MHz. The equipment allows for the ultrasonic measurements of spherical rock samples in 132 independent directions by using a pair of P-wave sensors (the transmitter and receiver are polarized along the radial direction). The 3D distribution of the P-wave velocities and amplitudes was analyzed in an angular grid of 15°.

## THEORY AND INVERSION METHOD

This section deals with methods used for determination of velocity and attenuation anisotropy from measured data on a spherical rock sample. The velocity and attenuation anisotropy is studied using a model of an anisotropic viscoelastic medium.

### Wave propagation in anisotropic viscoelastic medium

The anisotropic viscoelastic medium is described by complex-valued, frequency-dependent, viscoelastic parameters (Auld, 1973; Carcione, 2014). Their real and imaginary parts describe the elastic and attenuation anisotropy. The equations for waves in viscoelastic media are similar to those in elastic media except for being complex. Implementing complex algebra into equations is rather simple, but, still, some care is needed for understanding the physical meaning of the complex-valued quantities.

The wave propagation in anisotropic viscoelastic media has been studied by many authors. Properties of plane waves were analyzed, for example, by Carcione and Cavallini (1993), Deschamps et al. (1997), Shuvalov and Scott (1999), Deschamps and Assouline (2000), Červený and Pšenčík (2005, 2006), Zhu and Tsvankin (2006, 2007), and Rasolofosaon (2010). For the point sources, the wavefronts were analyzed, for example, by Carcione (1994); high-frequency wavefields were modeled by the ray method by Hearn and Krebes (1990), Gajewski and Pšenčík (1992), and Zhu and Chun (1994); and complete wavefields were computed by directly solving the wave equation by Carcione (1990, 1993) and Carcione et al. (1996). The exact and asymptotic Green's functions for a homogeneous medium were derived (Vavryčuk, 2007a), and some solutions of the complex eikonal equation for a special type of an inhomogeneous medium are reported (Vavryčuk, 2012). Methods for determining viscoelastic parameters from measured velocities and amplitudes of waves were developed by Vavryčuk (2015) and Vavryčuk et al. (2017).

## Basic formulas

A viscoelastic anisotropic medium is defined by density-normalized complex-valued and frequency-dependent stiffness parameters:

$$a_{ijkl} = c_{ijkl}/\rho, \quad (1)$$

where  $c_{ijkl}$  are the viscoelastic stiffness parameters and  $\rho$  is the density. The real and imaginary parts of  $a_{ijkl}$

$$a_{ijkl}(\omega) = a_{ijkl}^R + ia_{ijkl}^I, \quad (2)$$

define the elastic and viscous properties of the medium. The frequency dependence of the viscoelastic parameters is mostly due to the imaginary parts  $a_{ijkl}^I$ , and the real parts  $a_{ijkl}^R$  are usually assumed to be frequency independent (see Vavryčuk [2007a], his equation 2.5) or only slightly frequency dependent to satisfy the Kramers-Kronig relations. The Christoffel tensor  $\Gamma_{jk}$  is

$$\Gamma_{jk}(\mathbf{p}) = a_{ijkl}p_i p_l, \quad (3)$$

where  $\mathbf{p}$  is the slowness vector  $\mathbf{p} = \mathbf{n}/c$ ,  $c$  is the complex phase velocity, and  $\mathbf{n}$  is the complex slowness direction. From eigenvalues  $G$  and eigenvectors  $\mathbf{g}$  of the Christoffel tensor (for elastic media, see Červený [2001], his equation 2.2.34; for viscoelastic media, see Vavryčuk [2007b], his equation 10)

$$G(\mathbf{p}) = a_{ijkl}p_i p_l g_j g_k = 1, \quad (4)$$

we can calculate the complex phase velocity  $c$  that describes a propagation of plane waves in a homogeneous anisotropic medium. The determination of complex viscoelastic parameters  $a_{ijkl}$  from the complex phase velocity surface  $c = c(\mathbf{n})$  is a nonlinear inverse problem which can be solved using perturbation theory and iterations (see Sviitek et al., 2014; Vavryčuk, 2015).

In perturbation theory, we assume that the anisotropic medium defined by unknown parameters  $a_{ijkl}$  can be obtained by a small perturbation of a known reference medium:

$$a_{ijkl} = a_{ijkl}^0 + \Delta a_{ijkl}, \quad (5)$$

where  $a_{ijkl}^0$  defines the reference medium and  $\Delta a_{ijkl}$  its perturbation. Under this assumption, the equation for the square of the phase velocity  $c^2$  can be linearized as follows (Vavryčuk, 1997; Pšenčík and Vavryčuk, 2002; Sviitek et al., 2014):

$$\Delta c^2 = c^2 - c_0^2 = \Delta a_{ijkl} n_i n_l g_j^0 g_k^0, \quad (6)$$

where  $c_0$  and  $\mathbf{g}^0$  define the complex phase velocity and complex polarization vector in the reference medium,  $\Delta c^2$  is the misfit between the squared phase velocity calculated from measurements and from the velocity in the reference medium. Using perturbations  $\Delta a_{ijkl}$ , we obtain parameters  $a_{ijkl}$  by equation 5. The calculated medium serves as the reference medium in the next iteration. The iterations are repeated until perturbations  $\Delta a_{ijkl}$  are negligibly small.

## Inversion strategy

In this work, we use measurements of velocities and amplitudes of P-waves; thus, only 15 viscoelastic parameters can be established with a satisfactory precision (Vavryčuk, 2009; Sviitek et al., 2014). Because the emitter of the ultrasonic waves is much smaller than the size of the rock sample, the waves can be considered to be generated by a point-like source. In this case, the ray quantities are measured (Vavryčuk, 2007b) and have to be recalculated to the phase quantities before inverting them for parameters of viscoelastic anisotropy. In addition, amplitudes measured on the spherical sample are affected by several factors of different origins: (1) the quality of the contact between the sample and transducer, (2) the radiation pattern of a point source in an anisotropic rock, (3) the geometric spreading of waves, and (4) the decay of amplitudes due to anisotropic attenuation. Therefore, the measured amplitudes must be corrected and effects (1–3) properly eliminated to deal with the effect of anisotropic attenuation only.

The individual steps of the inversion for anisotropic viscoelastic parameters are as follows:

- Parameters  $a_{ijkl}^R$  of elastic anisotropy of a rock are determined from measurements of the ray velocity  $V^{\text{ray}}$  (see Sviitek et al., 2014).
- Measured amplitudes are calibrated for a quality of the contact between the sample and transducer using independent measurements on a spherical sample of glass.
- The radiation pattern and geometric spreading of elastic waves propagating in the anisotropic rock are calculated (Vavryčuk, 2007a; Vavryčuk et al. [2017], their equation 16).
- The measured amplitude decay of the signal is corrected for the radiation pattern of a point source in the anisotropic rock and for geometric spreading. The corrected value is normalized to a unit ray length.
- Having calculated ray velocity  $V^{\text{ray}}$  and ray attenuation  $A^{\text{ray}}$ , we determine the inverse of the complex energy velocity  $v$  for a set of ray directions  $\mathbf{N}$  as follows (see Vavryčuk et al. [2017], their equation 8):

$$\frac{1}{v} = \frac{1}{V^{\text{ray}}} + iA^{\text{ray}}. \quad (7)$$

- We construct the complex energy velocity surface for ray directions  $\mathbf{N}$ :

$$v = v(\mathbf{N}). \quad (8)$$

- Using the reciprocity equation (for elastic media, see Musgrave [1970], his equation 7.4.1a; for viscoelastic media, see Vavryčuk [2007b], his equation 12)

$$\mathbf{v} \cdot \mathbf{p} = 1, \quad (9)$$

the complex phase velocity surface is constructed for a set of slowness directions  $\mathbf{n}$  (for details, see Appendix A):

$$c = c(\mathbf{n}). \quad (10)$$

- The calculated elastic anisotropy parameters are used for defining the reference medium. We invert for 15 weak-anisotropy-attenuation (WAA) parameters from the complex

WA36

Svitek et al.

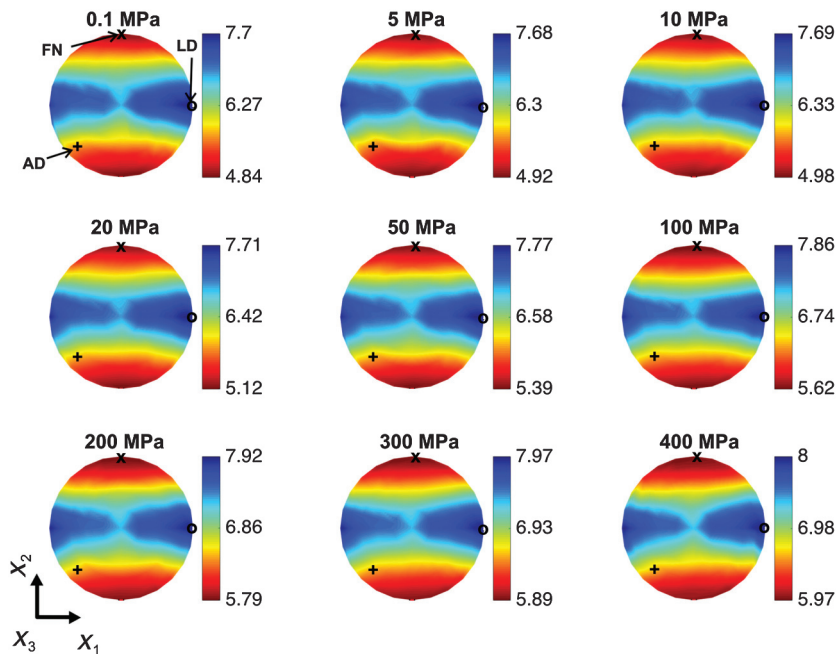


Figure 1. The 3D P-wave velocity distribution (in km/s) measured at nine pressure levels in the range of 0.1–400 MPa. The 2D projection is used, where the coordinates of points inside the circles are the  $x_1$  and  $x_2$  components of the direction vector. This defines the orthographic projection with the viewpoint ( $90^\circ, 0^\circ$ ). The viewpoint notation is specified by two angles (azimuth and elevation), where ( $90^\circ, 0^\circ$ ) corresponds to axis  $+x_1$  pointing right,  $+x_2$  pointing up, and  $+x_3$  pointing to spectator. For a definition of the directions LD, FN, and AD, see the text.

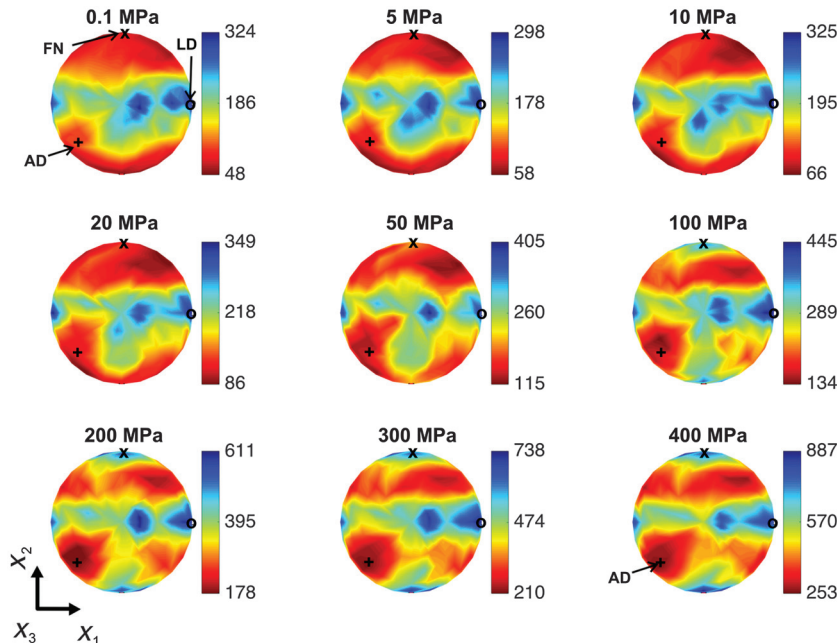


Figure 2. The 3D amplitude distribution (in mV) projected on the spherical surface, measured at nine pressure levels in the range of 0.1–400 MPa. Viewpoint ( $90^\circ, 0^\circ$ ). For details of the projection, see the caption of Figure 1. For a definition of the directions LD, FN, and AD, see the text.

phase velocity surface using equation 30 of Vavryčuk et al. (2017). The remaining six WAA parameters describing the triclinic viscoelastic anisotropy are related to propagation of S-waves and cannot be retrieved from P-wave measurements. This does not pose any difficulty because the predicted P-wave quantities are not sensitive to them.

- Finally, the obtained viscoelastic parameters are used for calculating the theoretical complex phase and energy velocities  $c$  and  $v$ , and subsequently for calculating attenuations and  $Q$ -factors:

$$A^{\text{phase}} = -\frac{c^I}{c^R c^R + c^I c^I},$$

$$A^{\text{ray}} = -\frac{v^I}{v^R v^R + v^I v^I}, \quad (11)$$

$$Q^{\text{phase}} = -\frac{(c^2)^R}{(c^2)^I},$$

$$Q^{\text{ray}} = -\frac{(v^2)^R}{(v^2)^I}, \quad (12)$$

where  $v = \sqrt{v_i v_i}$  and  $c = 1/\sqrt{p_i p_i}$ .

For a detailed description of the inversion method, see Vavryčuk et al. (2017), in which the method was also numerically tested on synthetic as well as experimental data.

## RESULTS

Figures 1 and 2 show the measured ultrasonic P-wave velocities and amplitudes on the spherical sample at nine pressure levels in the range of 0.1–400 MPa. The data were measured in 132 independent directions in the regular  $15^\circ$  grid. The velocities (in km/s) and amplitudes (in mV) were measured on the same waveforms. The directional distribution of velocities in Figure 1 shows a high-velocity plane (foliation plane) with the maximum velocity oriented in this plane (lineation direction) and one main region of low velocities perpendicular to the foliation plane. This pattern suggests anisotropy close to orthorhombic (orthotropic) symmetry. Based on Figures 1 and 2, three significant directions are selected to describe and compare results obtained by high-pressure experiment on the spherical sample. The values measured at 400 MPa were considered at the selection: (1) LD — lineation direction (maximum velocity direction), (2) FN — foliation normal (defined as the normal to the foliation plane, minimum velocity direction), and (3) AD — amplitude direction (direction of the minimum amplitude at 400 MPa).

Figure 1 shows that the velocity distribution over the spherical surface is stable through all pressure levels. No change in anisotropy orientation and in its symmetry is observed. The velocity distribution shows one significant plane of high velocities with maximum oriented in one single direction. On the contrary, the area of minimum velocities is oriented perpendicular to this layer. The maximum velocities increase with pressure by approximately 300 m/s whereas the increase in the minimum velocities is more than 1000 m/s. Consequently, strength of velocity anisotropy decreases with increasing pressure.

The amplitudes measured on the rock sample are sensitive to a contact between the sample and transducers. Because this contact can differ at individual pressure levels, it must be calibrated and the amplitude measurements corrected. Calibration of the contact conditions between the spherical sample and pair of transducers was performed on an amorphous glass sphere with a diameter of 50 mm, subjected to hydrostatic pressure from 0.1 to 400 MPa. Because no velocity change was observed in all directions in this range of pressure, we can deduce that the observed increase of amplitudes reflects the change of the contact between the sample and transducers. The amplitudes measured at 400 MPa were three times higher than those measured at 0.1 MPa. The increase was approximately linear from 5 MPa. Consequently, the amplitudes measured on the serpentinite sample were corrected to eliminate the effect of a different contact between the sample and transducers at each pressure level.

The directional distribution of amplitudes at low pressures (see Figure 2) is similar to the distribution of velocities. Maximum amplitudes are observed in the foliation plane and correlate with the maximum velocities. However, in contrast to the velocity distribution, which is quite stable for all pressure levels, the amplitude dis-

tribution displays remarkable changes through individual pressure levels. These changes are mostly observed in directions close to the foliation normal (FN). The amplitudes significantly increase with increasing pressure and form a new local maximum for pressures greater than 100 MPa. This might be caused by the closure of micro-cracks, which leads to a change of friction conditions and results in a decrease in signal attenuation. The lowest amplitudes are observed in the FN direction at low pressure. However, the direction of the lowest amplitude changes by acting pressure. Consequently, this direction is inclined by  $45^\circ$  from the foliation plane at 400 MPa.

Figure 3 shows the measured velocities (a and e), measured amplitudes (b and f), calculated normalized radiation pattern (c and g), and calculated  $Q$ -factors (d and h) at 0.1 and 400 MPa, respectively. The normalized radiation pattern is calculated according to equation 16 of Vavryčuk et al. (2017) for a point source in an elastic anisotropic rock described by parameters inverted from measured velocities in Figure 3a and 3e. We selected a different viewpoint in Figure 3, to better identify a behavior of individual quantities in the LD, FN, and AD directions. The black dots on the spherical surface mark points of measurements, and the white letters mark the selected directions. The velocities, amplitudes, and  $Q$ -factors in these directions are studied in detail in the following text. The radiation pattern (RP) shows the effect of the velocity anisotropy on amplitudes radiated by a point source. The RP in Figure 3c is calculated through the Green's function of the elastic anisotropy retrieved from the velocity distribution (Figure 3a). The  $Q$ -factor (Figure 3d) is then calculated from the amplitude distribution (Figure 3b) corrected to RP (Figure 3c).

Figure 4 shows the variation of the P-wave velocities with pressure in selected directions. The exponential increase in the minimum velocity for pressures up to 100 MPa suggests closing of

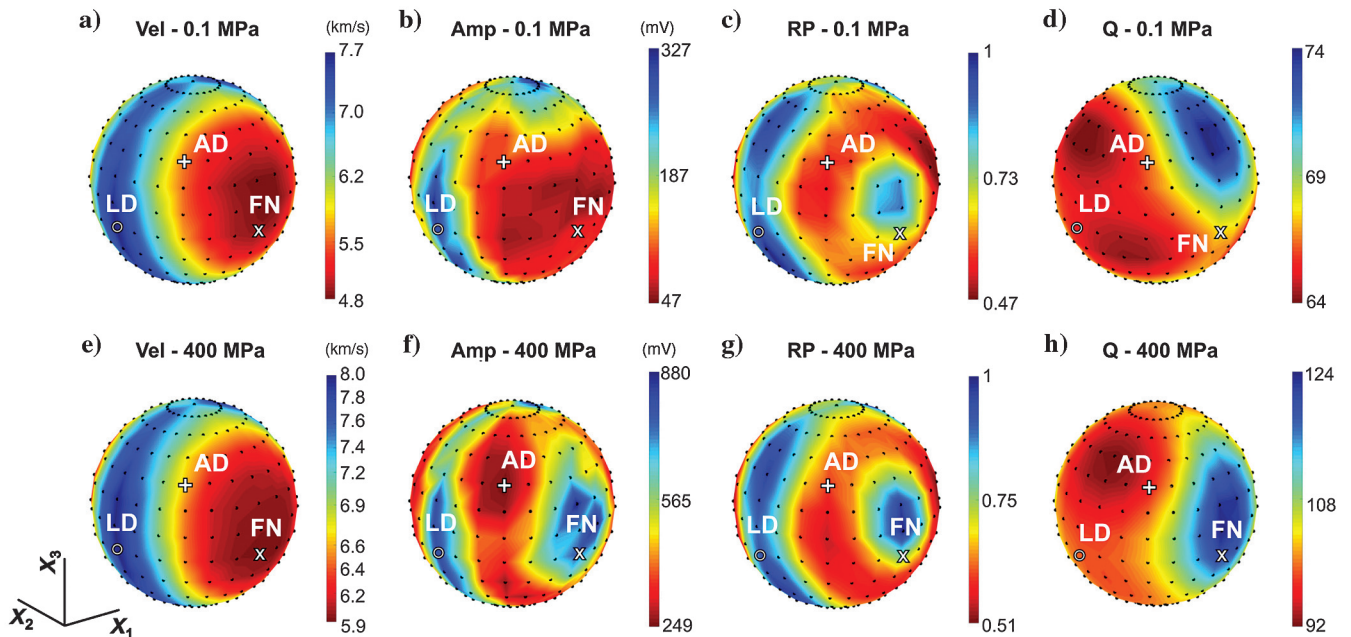


Figure 3. (a and e) The 3D projection on the spherical surface of measured velocities, (b and f) amplitudes, (c and g) calculated normalized radiation pattern (RP), and (d and h) ray  $Q$ -factors at 0.1–400 MPa, respectively. The black dots represent points of measurement, and the white letters mark the selected directions — lineation (LD), foliation normal (FN), and amplitude minimum (AD). The positions of the LD, FN, and AD directions are marked by the circle, cross, and plus signs, respectively. The  $x_1$ ,  $x_2$ , and  $x_3$  axes show the orientation of the sample. Viewpoint ( $-40^\circ$ ,  $20^\circ$ ).

microcracks oriented perpendicular to the minimum velocity direction (FN). The trend of this line remains quasilinear at pressures greater than 100 MPa. The trend of the maximum velocity (LD) is quasilinear in the whole range of pressures. This indicates that no microcracks are aligned in the direction perpendicular to the direction of the maximum velocity (LD). According to the velocity dependence in the main structural directions, the rock sample exhibits a crack preferred orientation only in the direction parallel to the foliation plane. The effect of crack closure and rock compaction is also expressed by a reduction of the strength of the velocity anisotropy from 46% to 29% at 0.1 and 400 MPa, respectively. A coefficient of anisotropy (in percent) is calculated using the following equation:

$$k = 200 \frac{d_{\max} - d_{\min}}{d_{\max} + d_{\min}}, \quad (13)$$

where  $d_{\max}$  and  $d_{\min}$  are the global extremes of the quantity  $d$  over all directions. This formula is used for calculation of the velocity, amplitude, and the  $Q$ -factor anisotropy. The velocity anisotropy strength

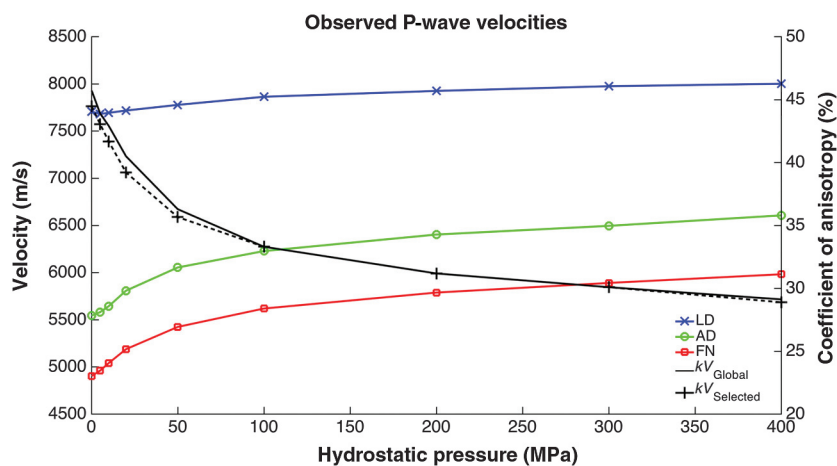


Figure 4. Measured P-wave velocities in three selected directions and coefficients of anisotropy  $kV_{\text{Selected}}$  and  $kV_{\text{Global}}$  as a function of pressure. The errors in velocities are estimated to be approximately 2% (Vavryčuk et al., 2017).

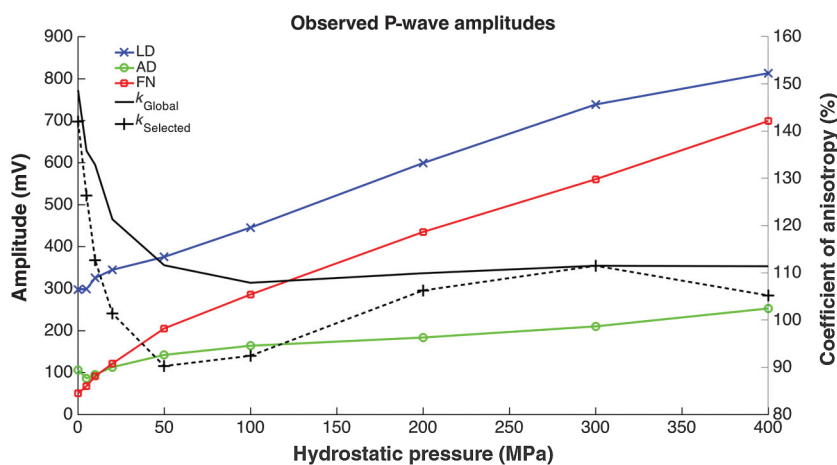


Figure 5. Measured P-wave amplitudes in three selected directions and coefficient of anisotropy  $kA_{\text{Selected}}$  and  $kA_{\text{Global}}$  as a function of pressure. The errors in amplitudes are estimated to be approximately 10% (Vavryčuk et al., 2017).

is quantified in Figure 4 by two coefficients: (1)  $kV_{\text{Global}}$  — calculated from the global velocity maximum and minimum, and (2)  $kV_{\text{Selected}}$  — calculated from velocities in the selected directions. Both lines are almost identical which means that the selected directions mostly coincide with the global maximum and minimum. The third direction, selected as the direction of the minimum amplitude (AD) measured at 400 MPa, is associated with no anomaly in the velocity distribution and looks like a regular direction in the velocity pattern. No significant changes of velocity are observed in the AD direction through individual pressure levels.

As indicated in Figure 5, the variation of measured amplitudes with pressure is slightly different than the variation of velocities. The amplitude increase with pressure is roughly linear for values greater than 50–100 MPa, but the increase has a significantly different rate in the selected directions. The increase in amplitudes in the AD direction is much lower than in the LD and FN directions. Because the amplitude in FN is lower than in AD at 0.1 MPa and the amplitude increase in FN is quite strong, the AD and FN curves intersect (at approximately 15 MPa). The low increase in amplitudes in the AD direction causes that this direction becomes the global minimum at high pressure. A complex behavior of amplitudes in the selected directions is reflected in the variation in the coefficient of anisotropy: (1)  $kA_{\text{Global}}$  — calculated from the global amplitude maximum and minimum, and (2)  $kA_{\text{Selected}}$  — calculated from amplitudes in the selected directions. Contrary to velocities, the extremes of amplitudes migrate to different positions with the pressure rising. This is the reason why the curves of  $kA_{\text{Global}}$  and  $kA_{\text{Selected}}$  do not coincide.

Figures 6 and 7 show the P-waveforms recorded in directions LD, FN, and AD at different pressure levels. In the LD direction (Figure 6a), the arrival time of the P-waves decreases only slightly with the increasing pressure from 6.5 to 6.0  $\mu\text{s}$ . At high pressure levels, a high-frequency undulation is visible. Amplitudes of the high-frequency signal start growing at the pressure level of 100 MPa when most of the cracks oriented perpendicular to the LD direction are closed. The observed frequency coincides with the resonance frequency of the transmitter. This frequency is suppressed at low pressure because of the scattering of waves by microcracks and grain boundaries and attenuation. The low-frequency signal reflects structural/textural inhomogeneities on a large scale and multiple reflections from the surface of the sample.

The arrival time of the P-waves in the FN direction (Figure 6b) decreases more strongly with pressure from 10.2 to 8.5  $\mu\text{s}$ , which corresponds to the minimum velocity in Figure 4. In comparison with the LD, a strong filtering of all frequencies can be seen at low pressure. This is due to a system of microcracks oriented perpendicular to the FN, which are open at low pressures (less than 100 MPa) and the energy of the signal attenuates significantly. However, the contact among mineral

grains improves with pressure; thus, more energy can be transferred along the trace. Consequently, the high-frequency content of the signals increases with the increasing pressure.

A comparison of waveforms recorded in three selected directions at all pressure levels is shown in Figure 7. The blue, green, and red curves show waveforms in the LD, AD, and FN directions, respectively. Although high-voltage crosstalk is visible at the beginning of each signal, the P-wave signals are not affected. The effect of anisotropy on velocity and attenuation is clearly visible in individual directions and at various pressure levels. Similarly, the differences in behavior of velocities and amplitudes in relation to the intrinsic structure of the rock material are well pronounced. One could expect small amplitudes of the signal in the slow direction (FN); however, once microcracks are closed, the amplitudes in the FN direction are almost of the same size as in the fast direction (LD). On the contrary, the AD direction is characterized by a moderate velocity, even though the amplitudes are minimal. This direction is oriented approximately by  $45^\circ$  to the foliation plane.

Figure 8 presents the directional variation of the  $Q$ -factor at pressure levels 0.1–400 MPa calculated based on the method described in section 3. The  $Q$ -factor distribution is changed with the pressure in the shape and in the symmetry orientation. The variation of the  $Q$ -factor over the spherical sample is rather small at low pressure. However, the  $Q$ -factor increases as well as the difference between its maximum and minimum values with pressure. This is caused by the closure of microcracks leading to improvement of contact conditions (internal friction) among mineral grains, so the transfer of energy is more efficient.

The increase of the  $Q$ -factor variation with pressure is reflected in strength of the  $Q$ -factor anisotropy. Figure 9 shows the development of the  $Q$ -factor with pressure in the LD (blue), FN (red), and AD (green) together with the coefficient of anisotropy calculated from the global maximum and minimum ( $kQ_{\text{Global}}$ ) and from the values in the selected directions ( $kQ_{\text{Selected}}$ ) using equation 13. The trend of both curves is rising with pressure, which is opposite to the trend of the velocities and amplitudes shown in Figures 4 and 5, respectively. Although the  $kQ_{\text{Global}}$  and  $kQ_{\text{Selected}}$  curves are parallel to each other, the relation between them suggests that the selected directions LD, FN, and AD do not coincide with the global maximum and minimum. The gray triangles and squares in Figure 9 show data of [Kem et al. \(1997\)](#), their figure 6) measured in directions parallel to the lineation and normal to the foliation plane, which should correspond to the LD and FN

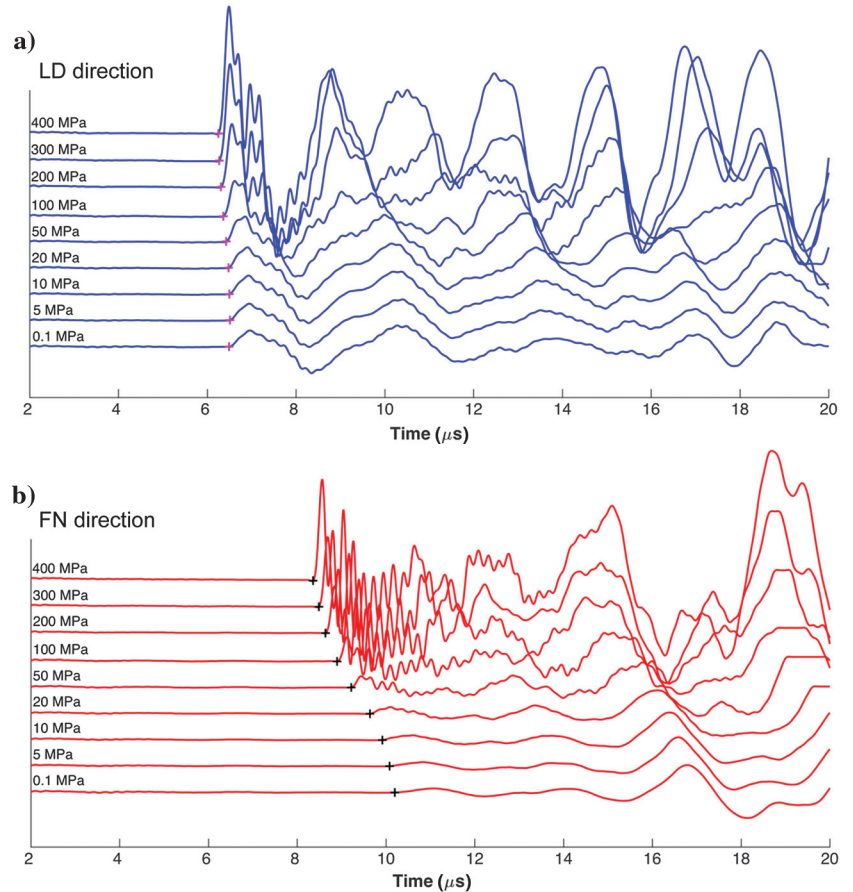


Figure 6. P-waveforms at individual pressure levels recorded in the (a) LD and (b) FN directions. The FN direction coincides with the normal to the system of microcracks.

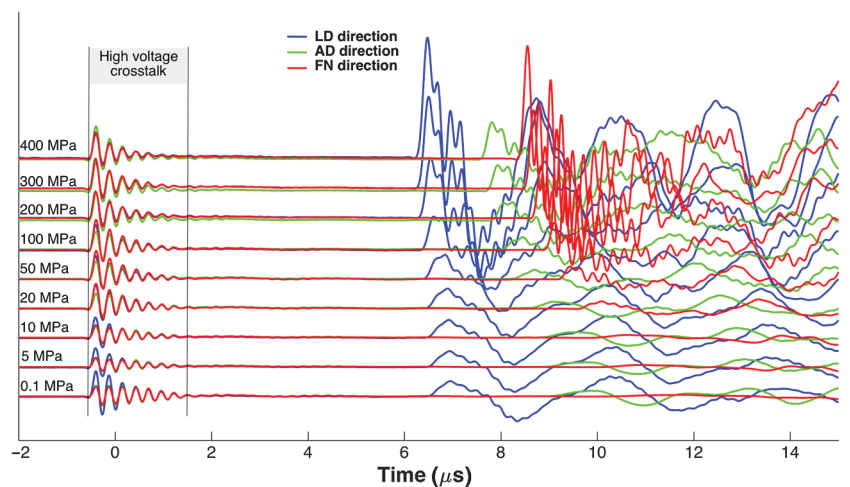


Figure 7. A comparison of waveforms recorded at individual pressure levels in selected directions: parallel to lineation (LD, blue), perpendicular to foliation, layers, and microcracks (FN, red), and the minimum of amplitudes at 400 MPa (AD, green). A high-voltage crosstalk between the transmitter and the receiver is visible at the beginning of the signals. All signals are plotted with the same sensitivity.

directions, respectively. Because both data sets were measured on different samples and the  $Q$ -factor was calculated using different methods, the results of Kern et al. (1997) are slightly different. The heterogeneity of the material might also play an important role.

DISCUSSION

Kern et al. (1997) describe the relation between the serpentinite texture and anisotropy of velocity and attenuation based on the

ultrasonic sounding in three mutually perpendicular directions. In the presented experiment, the velocity and amplitudes are measured in 132 independent directions, which are distributed over the spherical surface of the sample. The dense coverage of directions is necessary for a detailed monitoring of changes in the orientation of velocity and amplitude anisotropy, and for the inversion for accurate anisotropy-attenuation parameters. Note that retrieving the velocity and attenuation anisotropy complicates two factors: First, the measured ray quantities must be recalculated to the phase quantities, and, second, the measured amplitudes must be corrected for the radiation pattern of elastic waves propagating in the anisotropic rock before the inversion.

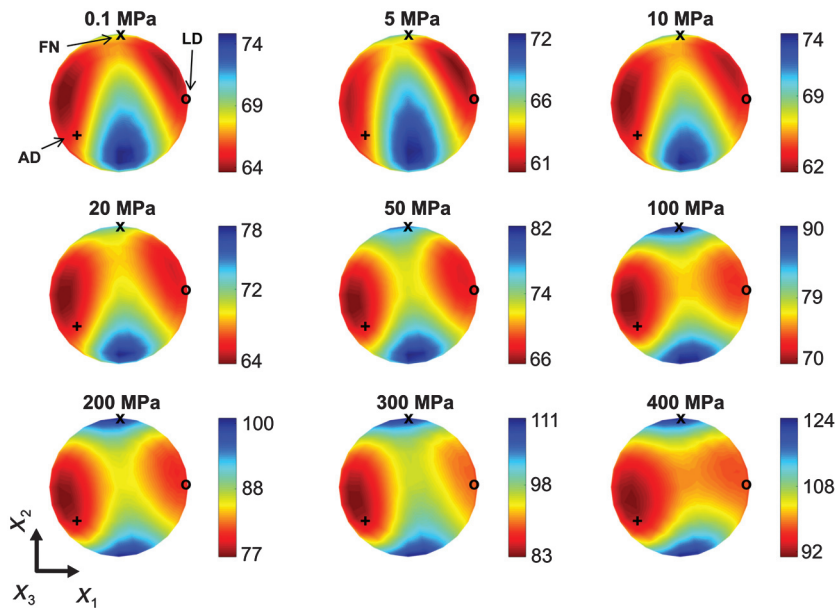


Figure 8. The P-wave ray  $Q$ -factor calculated for nine pressure levels in the range of 0.1–400 MPa. Viewpoint ( $90^\circ, 0^\circ$ ). For details of the projection, see the caption of Figure 1. Directions LD, FN, and AD are marked by the circle, cross, and plus signs, respectively.

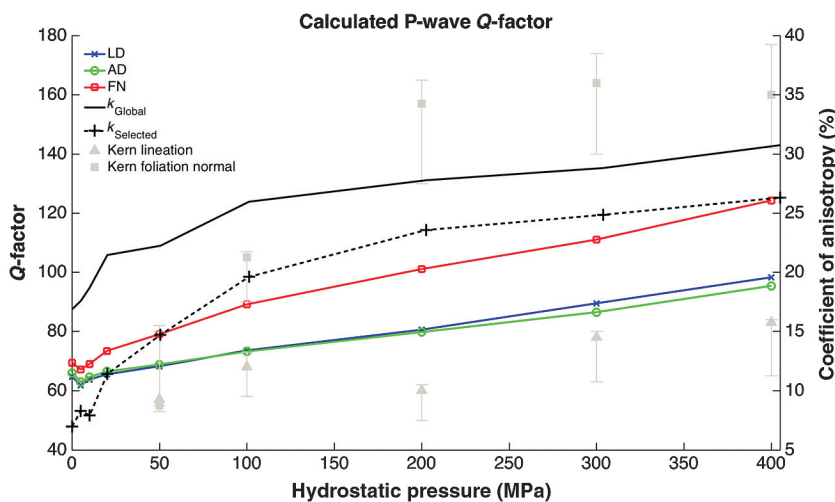


Figure 9. Dependence of the calculated P-wave  $Q$ -factors on pressure in three selected directions: LD, blue; AD, green; FN, red; and their coefficient of anisotropy  $kQ_{Global}$ , calculated from the global extremes, black full and  $kQ_{Selected}$ , calculated from values in the selected directions, black dotted. The gray squares and triangles denote data of Kern et al. (1997). The errors in the  $Q$ -factors are estimated to be approximately 10% (Vavryčuk et al., 2017).

and, second, the measured amplitudes must be corrected for the radiation pattern of elastic waves propagating in the anisotropic rock before the inversion.

The P-wave velocity distribution shows strong anisotropy resulting from CPO of constituent minerals, compositional banding, and the spatial variation of modal composition. The pressure dependence of the P-wave velocity can be divided into two parts of a different character (Pros et al., 1998; Ullemeyer et al., 2011): (1) an exponential increase of velocity from 0.1 to 100 MPa, mainly due to the microcrack closure, and (2) a linear increase of velocity from 100 to 400 MPa, due to the pressure influence on the intrinsic velocity of the rock fabric (see Figure 4). The strong intrinsic velocity anisotropy ( $k \sim 30\%$ ) reflects the alignment of platy antigorite minerals, which constitute approximately 75 vol% of the serpentinite (Kern et al., 1997). The fact that the presence of microcracks increases anisotropy (approximately by 10%) without changing its orientation (Figure 1), may be explained by the active role of the antigorite grain boundaries, which form a microcrack system parallel to the foliation. This interpretation is in accordance with the photomicrograph of antigorite grain boundaries published in Kern et al. (1997). The velocities measured in the FN and AD directions are influenced by these microcracks, whereas the LD is almost crack free (Figure 4).

The P-wave velocities measured on the sphere in the three orthogonal structural directions compare fairly well with those measured by Kern (1993) and Kern et al. (1997) on sample cubes of the antigorite serpentinite. The same holds for the anisotropy of the P-wave velocities. Also, the calculated P-wave velocities based on the CPOs of antigorite obtained by the synchrotron and neutron diffraction are in reasonable agreement with the experimental data.

Due to the point contact between the ultrasonic sensors and the tested specimen, the ray velocity is measured in this experimental setup. The measured amplitude response is then a combination of two effects: (1) the elastic radiation pattern (RP) of the point source generating the ultrasonic waves and (2) the anelastic attenuation. To obtain the  $Q$ -factor, the measured amplitudes must be corrected for the RP effect. The fact that the cor-

rection itself resembles the measured amplitude anisotropy (compare Figure 3f and 3g) illustrates the strong influence of RP on amplitudes and demonstrates a significance of the correction. A different character of waveforms in the symmetry axis (FN, LD; no influence of RP) compared with the waveforms in AD as well as the amplitude-pressure relation in the mentioned directions (Figure 5) reflects the effect of RP.

The  $Q$ -factor anisotropy increases in the entire pressure interval. With the increasing pressure, the effect of the grain contact sliding decreases and the  $Q$ -factor is more influenced by the intrinsic properties of the rock fabric. The progressive closure of the microcracks causes rotation of the axes of the  $Q$ -factor anisotropy. At pressures greater than 100 MPa, the orientation of the  $Q$ -factor anisotropy does not further change. Surprisingly, the maximum values correspond to the FN direction, where minimum velocities are observed, whereas the low values lie in the foliation plane. Kern et al. (1997) report a very similar behavior of the  $Q$ -factor and the velocity pressure dependence measured on the same rock type in the three structural mutually perpendicular directions. This indicates that the common correlation between high velocities and high  $Q$ -factor directions known for cracked media (Hudson, 1981, 1990) does not apply to rocks with intrinsic anisotropy. In this case, the relation between the velocity and  $Q$ -factor anisotropy is more complex.

We focused on the 3D distribution of the P-wave velocity and attenuation. A complete description of the viscoelastic behavior of rocks needs additional measurements of the corresponding S-wave quantities. They are particularly needed for determining accurately the so-called S-wave-related viscoelastic parameters:  $a_{44}$ ,  $a_{55}$ ,  $a_{66}$ ,  $a_{45}$ ,  $a_{46}$ , and  $a_{56}$ . Incorporating the S-wave velocities in the inversion for elastic parameters is reported in Svitek et al. (2014), and measurements of the S-wave amplitudes and attenuation are under way. The inversion of the S-wave quantities for the viscoelastic parameters will also need further theoretical developments. Specifically, recalculating the ray to phase quantities will be more involved for the S-waves than for the P-waves because of the frequently observed S-wave triplications and caustics (Vavryčuk, 2003).

## CONCLUSION

This paper presents the analysis of the P-wave velocity and amplitude data measured on a spherical sample of serpentinite rock at nine pressure levels from 0.1 to 400 MPa. The conclusions of this investigation can be summarized as follows:

- The multidirectional ultrasonic measurement of the spherical sample can be used for determining the velocity and attenuation anisotropy in rocks and their intrinsic or extrinsic origins.
- At pressures greater than 100 MPa, where the microcracks are already closed, the measured amplitude anisotropy strongly reflects the point source radiation pattern of elastic waves propagating in the anisotropic rock. Therefore, the radiation pattern corrections are necessary to obtain the attenuation parameters.
- At low pressure, the intrinsic, CPO-caused velocity anisotropy (30%) is increased due to the effect of the grain boundary microcrack system (extrinsic anisotropy) up to the  $k = 45\%$ . The 30% intrinsic anisotropy of  $Q$  is diminished by the presence of microcracks to the value of  $k = 16\%$ .
- The orientation of the velocity anisotropy does not change with pressure, whereas the orientation of the  $Q$ -factor

anisotropy rotates for pressure in the range of 0–100 MPa. At pressures greater than 100 MPa, the high values of the  $Q$ -factor correspond to the direction perpendicular to foliation, whereas the low  $Q$ -factor follows the foliation plane.

## ACKNOWLEDGMENTS

We thank I. Ravve, S. Ji, Y. Soda, and two anonymous reviewers for their detailed and helpful reviews. This study was partly supported by research projects 13-13967S, 16-03950S, and 16-19751J with funding provided by the Grant Agency of the Czech Republic and by The Czech Academy of Sciences, project RVO 67985831.

## APPENDIX A

### CALCULATION OF COMPLEX PHASE VELOCITY

Inverting phase quantities for viscoelastic parameters is computationally much simpler than inverting ray quantities. Therefore, it is preferable to recalculate the complex energy velocity surface  $v(\mathbf{N})$  to the complex phase velocity surface  $c(\mathbf{n})$ , and then to perform the inversion. This can be done using the complex polar reciprocity relation 9 written in the following way:

$$\mathbf{v}^R \cdot \mathbf{p}^R - \mathbf{v}^I \cdot \mathbf{p}^I = 1, \quad (\text{A-1})$$

$$\mathbf{v}^R \cdot \mathbf{p}^I + \mathbf{v}^I \cdot \mathbf{p}^R = 0. \quad (\text{A-2})$$

In viscoelastic homogeneous media, the complex energy velocity vector  $\mathbf{v}$  has special properties. Because rays are straight lines and the source and receiver are situated in the real space, the rays are also real. As a consequence, the direction of the complex energy velocity vector is real, and the real and imaginary parts of vector  $\mathbf{v}$  are parallel. Vectors satisfying such property are called homogeneous. By contrast, complex slowness vector  $\mathbf{p}$  does not satisfy this condition being thus generally inhomogeneous. In viscoelastic inhomogeneous media, vectors  $\mathbf{v}$  and  $\mathbf{p}$  are inhomogeneous.

Because the complex energy velocity vector  $\mathbf{v}$  is homogeneous and the real and imaginary parts of the vector are parallel (see Vavryčuk 2007a), we can write

$$\mathbf{v}^R = v^R \mathbf{N}, \quad \mathbf{v}^I = v^I \mathbf{N}, \quad (\text{A-3})$$

where  $\mathbf{N}$  is the real ray direction. The complex slowness vector  $\mathbf{p}$  is generally inhomogeneous

$$\mathbf{p}^R = p^R \mathbf{s}^R, \quad \mathbf{p}^I = p^I \mathbf{s}^I, \quad (\text{A-4})$$

and  $\mathbf{s}^R$  and  $\mathbf{s}^I$  are real directions of vectors  $\mathbf{p}^R$  and  $\mathbf{p}^I$ , which are mutually different. Equations A-1 and A-2 imply

$$p^I = -\frac{v^I \mathbf{N} \cdot \mathbf{s}^R}{v^R \mathbf{N} \cdot \mathbf{s}^I} p^R, \quad (\text{A-5})$$

and consequently

$$p^R = \frac{v^R}{v^R v^R + v^I v^I} \frac{1}{\mathbf{N} \cdot \mathbf{s}^R}, \quad (\text{A-6})$$

$$p^I = -\frac{v^I}{v^R v^R + v^I v^I} \frac{1}{\mathbf{N} \cdot \mathbf{s}^I}. \quad (\text{A-7})$$

The complex slowness vector  $\mathbf{p}$  is calculated using equations A-6 and A-7 as

$$\mathbf{p} = p^R \mathbf{s}^R + i p^I \mathbf{s}^I, \quad (\text{A-8})$$

and its direction complex-valued direction  $\mathbf{n}$

$$\mathbf{n} = \frac{\mathbf{p}}{\sqrt{\mathbf{p} \cdot \mathbf{p}}}. \quad (\text{A-9})$$

Finally, the complex phase velocity surface  $c = c(\mathbf{n})$  is calculated as

$$c = v \mathbf{N} \cdot \mathbf{n}. \quad (\text{A-10})$$

The individual steps of calculating the complex phase velocity surface  $c = c(\mathbf{n})$  from the complex energy velocity surface  $v = v(\mathbf{N})$  can be summarized as follows. First, we interpolate ray velocity and amplitude measurements to get a sufficiently dense complex energy velocity surface  $v = v(\mathbf{N})$  using equations 7 and 8. Second, we calculate the real unit vectors  $\mathbf{s}^R$  and  $\mathbf{s}^I$  as the normals to the real part  $v^R = v^R(\mathbf{N})$  and to the imaginary part  $v^I = v^I(\mathbf{N})$  of the energy velocity surface  $v = v(\mathbf{N})$ . Because surfaces  $v^R = v^R(\mathbf{N})$  and  $v^I = v^I(\mathbf{N})$  are real, we can use standard formulas of differential geometry (Lipschutz, 1969). Third, we calculate  $p^R$  and  $p^I$  using equations A-6 and A-7, and subsequently the complex slowness vectors  $\mathbf{p}$  and its direction  $\mathbf{n}$  using equations A-8 and A-9. Finally, the complex phase velocity surface  $c = c(\mathbf{n})$  is obtained using equation A-10.

## REFERENCES

- Auld, B. A., 1973, *Acoustic fields and waves in solids*: Wiley.
- Babuška, V., 1984, P-wave velocity anisotropy in crystalline rocks: *Geophysical Journal of the Royal Astronomical Society*, **76**, 113–119, doi: [10.1111/j.1365-246X.1984.tb05026.x](https://doi.org/10.1111/j.1365-246X.1984.tb05026.x).
- Barruol, G., and H. Kern, 1996, Seismic anisotropy and shear-wave splitting in lower-crustal and upper-mantle rocks from the Ivrea Zone — Experimental and calculated data: *Physics of the Earth and Planetary Interiors*, **95**, 175–194, doi: [10.1016/0031-9201\(95\)03124-3](https://doi.org/10.1016/0031-9201(95)03124-3).
- Carcione, J. M., 1990, Wave propagation in anisotropic linear viscoelastic media: Theory and simulated wavefields: *Geophysical Journal International*, **101**, 739–750, doi: [10.1111/j.1365-246X.1990.tb05580.x](https://doi.org/10.1111/j.1365-246X.1990.tb05580.x).
- Carcione, J. M., 1993, Seismic modeling in viscoelastic media: *Geophysics*, **58**, 110–120, doi: [10.1190/1.1443340](https://doi.org/10.1190/1.1443340).
- Carcione, J. M., 1994, Wavefronts in dissipative anisotropic media: *Geophysics*, **59**, 644–657, doi: [10.1190/1.1443624](https://doi.org/10.1190/1.1443624).
- Carcione, J. M., 2014, *Wave fields in real media: Theory and numerical simulation of wave propagation in anisotropic, anelastic, porous and electromagnetic media*, 3rd ed.: Elsevier.
- Carcione, J. M., and F. Cavallini, 1993, Energy-balance and fundamental relations in anisotropic-viscoelastic media: *Wave Motion*, **18**, 11–20, doi: [10.1016/0165-2125\(93\)90057-M](https://doi.org/10.1016/0165-2125(93)90057-M).
- Carcione, J. M., G. Quiroga-Goode, and F. Cavallini, 1996, Wavefronts in dissipative anisotropic media: Comparison of the plane-wave theory with numerical modeling: *Geophysics*, **61**, 857–861, doi: [10.1190/1.1444010](https://doi.org/10.1190/1.1444010).
- Červený, V., 2001, *Seismic ray theory*: Cambridge University Press.
- Červený, V., and I. Pšenčík, 2005, Plane waves in viscoelastic anisotropic media — Part I: Theory: *Geophysical Journal International*, **161**, 197–212, doi: [10.1111/j.1365-246X.2005.02589.x](https://doi.org/10.1111/j.1365-246X.2005.02589.x).
- Červený, V., and I. Pšenčík, 2006, Energy flux in viscoelastic anisotropic media: *Geophysical Journal International*, **166**, 1299–1317, doi: [10.1111/j.1365-246X.2006.03057.x](https://doi.org/10.1111/j.1365-246X.2006.03057.x).
- Deschamps, M., and F. Assouline, 2000, Attenuation along the Poynting vector direction of inhomogeneous plane waves in absorbing and anisotropic solids: *Acta Acustica united with Acustica*, **86**, 295–302.
- Deschamps, M., B. Poiree, and O. Poncet, 1997, Energy velocity of complex harmonic plane waves in viscous fluids: *Wave Motion*, **25**, 51–60, doi: [10.1016/S0165-2125\(96\)00032-7](https://doi.org/10.1016/S0165-2125(96)00032-7).
- Gajewski, D., and I. Pšenčík, 1992, Vector wavefields for weakly attenuating anisotropic media by the ray method: *Geophysics*, **57**, 27–38, doi: [10.1190/1.1443186](https://doi.org/10.1190/1.1443186).
- Hacker, B. R., G. A. Abers, and S. M. Peacock, 2003a, Subduction factory — Part 1: Theoretical mineralogy, densities, seismic wave speeds, and H<sub>2</sub>O contents: *Journal of Geophysical Research*, **108**, 2029, doi: [10.1029/2001JB001127](https://doi.org/10.1029/2001JB001127).
- Hacker, B. R., S. M. Peacock, G. A. Abers, and S. D. Holloway, 2003b, Subduction factory — Part 2: Are intermediate-depth earthquakes in subducting slabs linked to metamorphic dehydration reactions?: *Journal of Geophysical Research*, **108**, 2030, doi: [10.1029/2001JB001129](https://doi.org/10.1029/2001JB001129).
- Hearn, D. J., and E. S. Krebes, 1990, On computing ray-synthetic seismograms for anelastic media using complex rays: *Geophysics*, **55**, 422–432, doi: [10.1190/1.1442851](https://doi.org/10.1190/1.1442851).
- Hudson, J. A., 1981, Wave speeds and attenuation of elastic waves in material containing cracks: *Geophysical Journal of the Royal Astronomical Society*, **64**, 133–150, doi: [10.1111/j.1365-246X.1981.tb02662.x](https://doi.org/10.1111/j.1365-246X.1981.tb02662.x).
- Hudson, J. A., 1990, Attenuation due to second-order scattering in material containing cracks: *Geophysical Journal International*, **102**, 485–490, doi: [10.1111/j.1365-246X.1990.tb04480.x](https://doi.org/10.1111/j.1365-246X.1990.tb04480.x).
- Jackson, I., J. D. Fitz Gerald, U. H. Faul, and B. H. Tan, 2002, Grain-size-sensitive seismic wave attenuation in polycrystalline olivine: *Journal of Geophysical Research, Solid Earth*, **107**, 2360, doi: [10.1029/2001JB001225](https://doi.org/10.1029/2001JB001225).
- Ji, S., A. Li, Q. Wang, C. Long, H. Wang, D. Marcotte, and M. Salisbury, 2013, Seismic velocities, anisotropy and shear-wave splitting in serpentinites and tectonic implications for subduction zones: *Journal of Geophysical Research*, **118**, 1015–1937, doi: [10.1002/jgrb.50110](https://doi.org/10.1002/jgrb.50110).
- Jung, H., 2011, Seismic anisotropy produced by serpentine in mantle wedge: *Earth and Planetary Science Letters*, **307**, 535–543, doi: [10.1016/j.epsl.2011.05.041](https://doi.org/10.1016/j.epsl.2011.05.041).
- Kern, H., 1993, P- and S-wave anisotropy and shear-wave splitting at pressure and temperature in possible mantle rocks and their relation to the rock fabric: *Physics of the Earth and Planetary Interiors*, **78**, 245–256, doi: [10.1016/0031-9201\(93\)90159-7](https://doi.org/10.1016/0031-9201(93)90159-7).
- Kern, H., B. Liu, and T. Popp, 1997, Relationship between anisotropy of P and S wave velocities and anisotropy of attenuation in serpentinite and amphibolites: *Journal of Geophysical Research*, **102**, 3051–3065, doi: [10.1029/96JB03392](https://doi.org/10.1029/96JB03392).
- Kern, H., T. Lokajčiček, T. Svitek, and H.-R. Wenk, 2015, Seismic anisotropy of serpentinite from Val Malenco, Italy: *Journal of the Geophysical Research, Solid Earth*, **120**, 4113–4129, doi: [10.1002/2015JB012030](https://doi.org/10.1002/2015JB012030).
- Klíma, K., J. S. Reinhardt, J. Vaněk, M. Aurberger, and Z. Pros, 1962, Ultrasonic attenuation of longitudinal waves in solids: *Journal of the Geophysical Research*, **67**, 2078–2080, doi: [10.1029/JZ067i005p02078](https://doi.org/10.1029/JZ067i005p02078).
- Klíma, K., J. Vaněk, and Z. Pros, 1964, The attenuation of longitudinal waves in diabase and greywacke under pressures up to 4 kilobars: *Studia Geophysica et Geodaetica*, **8**, 247–254, doi: [10.1007/BF02060825](https://doi.org/10.1007/BF02060825).
- Lipschutz, M., 1969, *Differential geometry*: McGraw-Hill.
- Lokajčiček, T., and T. Svitek, 2015, Laboratory measurement of elastic anisotropy on spherical rock samples by longitudinal and transverse sounding under confining pressure: *Ultrasonics*, **56**, 294–302, doi: [10.1016/j.ultras.2014.08.015](https://doi.org/10.1016/j.ultras.2014.08.015).
- Musgrave, M. J. P., 1970, *Crystal acoustics*: Holden-Day.
- Pros, Z., T. Lokajčiček, and K. Klíma, 1998, Laboratory approach to the study of elastic anisotropy on rock samples: *Pure and Applied Geophysics*, **151**, 619–629, doi: [10.1007/s000240050133](https://doi.org/10.1007/s000240050133).
- Pšenčík, I., and V. Vavryčuk, 2002, Approximate relation between the ray vector and wave normal in weakly anisotropic media: *Studia Geophysica et Geodaetica*, **46**, 793–807, doi: [10.1023/A:1021189724526](https://doi.org/10.1023/A:1021189724526).
- Rasolofosaon, P. N. J., 2010, Generalized anisotropy parameters and approximations of attenuations and velocities in viscoelastic media of arbitrary anisotropy type — Theoretical and experimental aspects: *Geophysical Prospecting*, **58**, 637–655, doi: [10.1111/j.1365-2478.2009.00863.x](https://doi.org/10.1111/j.1365-2478.2009.00863.x).
- Shao, T., S. Ji, Y. Kondo, K. Michibayashi, Q. Wang, Z. Xu, S. Sun, D. Marcotte, and H. M. Salisbury, 2014, Antigorite-induced seismic anisotropy and implications for deformation in subduction zones and the Tibet Plateau: *Journal of the Geophysical Research, Solid Earth*, **119**, 2068–2099, doi: [10.1002/2013JB010661](https://doi.org/10.1002/2013JB010661).
- Shuvalov, A. L., and N. H. Scott, 1999, On the properties of homogeneous viscoelastic waves: *The Quarterly Journal of Mechanics and Applied Mathematics*, **52**, 405–417, doi: [10.1093/qjmath/52.3.405](https://doi.org/10.1093/qjmath/52.3.405).
- Svitek, T., V. Vavryčuk, T. Lokajčiček, and M. Petružálek, 2014, Determination of elastic anisotropy of rocks from P- and S-wave velocities: Numerical modelling and lab measurements: *Geophysical Journal International*, **199**, 1682–1697, doi: [10.1093/gji/ggu332](https://doi.org/10.1093/gji/ggu332).

- Ullmeyer, K., D. I. Nikolayev, N. I. Christensen, and J. H. Behrmann, 2011, Evaluation of intrinsic velocity — Pressure trends from low-pressure P-wave velocity measurements in rock containing microcracks: *Geophysical Journal International*, **185**, 1312–1320, doi: [10.1111/j.1365-246X.2011.05008.x](https://doi.org/10.1111/j.1365-246X.2011.05008.x).
- Ulmer, P., and V. Trommsdorff, 1995, Serpentine stability to mantle depth and subduction-related magmatism: *Science*, **268**, 858–861, doi: [10.1126/science.268.5212.858](https://doi.org/10.1126/science.268.5212.858).
- Vavryčuk, V., 1997, Elastodynamic and elastostatic Green tensors for homogeneous weak transversely isotropic media: *Geophysical Journal International*, **130**, 786–800, doi: [10.1111/j.1365-246X.1997.tb01873.x](https://doi.org/10.1111/j.1365-246X.1997.tb01873.x).
- Vavryčuk, V., 2003, Parabolic lines and caustics in homogeneous weakly anisotropic solids: *Geophysical Journal International*, **152**, 318–334, doi: [10.1046/j.1365-246X.2003.01845.x](https://doi.org/10.1046/j.1365-246X.2003.01845.x).
- Vavryčuk, V., 2007a, Asymptotic Green's function in homogeneous anisotropic viscoelastic media: *Proceedings of the Royal Society A*, **463**, 2689–2707, doi: [10.1098/rspa.2007.1862](https://doi.org/10.1098/rspa.2007.1862).
- Vavryčuk, V., 2007b, Ray velocity and ray attenuation in homogeneous anisotropic viscoelastic media: *Geophysics*, **72**, no. 6, D119–D127, doi: [10.1190/1.2768402](https://doi.org/10.1190/1.2768402).
- Vavryčuk, V., 2009, Weak anisotropy-attenuation parameters: *Geophysics*, **74**, no. 5, WB203–WB213, doi: [10.1190/1.3173154](https://doi.org/10.1190/1.3173154).
- Vavryčuk, V., 2012, On numerically solving the complex eikonal equation using real ray-tracing methods: A comparison with the exact analytical solution: *Geophysics*, **77**, no. 4, T109–T116, doi: [10.1190/geo2011-0431.1](https://doi.org/10.1190/geo2011-0431.1).
- Vavryčuk, V., 2015, Determination of parameters of viscoelastic anisotropy from ray velocity and ray attenuation: Theory and numerical modeling: *Geophysics*, **80**, no. 3, C59–C71, doi: [10.1190/geo2014-0355.1](https://doi.org/10.1190/geo2014-0355.1).
- Vavryčuk, V., T. Svitek, and T. Lokajčiek, 2017, Anisotropic attenuation in rocks: Theory, modelling and lab measurements: *Geophysical Journal International*, **208**, 1724–1739, doi: [10.1093/gji/ggw476](https://doi.org/10.1093/gji/ggw476).
- Watanabe, T., H. Kasami, and S. Ohshima, 2007, Compressional and shear wave velocities of serpentized peridotites up to 200 MPa: *Earth Planets Space*, **59**, 233–244, doi: [10.1186/BF03353100](https://doi.org/10.1186/BF03353100).
- Watanabe, T., Y. Shirasugi, and K. Michibayashi, 2014, A new method for calculating seismic velocities in rocks containing strongly dimensionally anisotropic mineral grains and its application to antigorite-bearing serpentinite mylonites: *Earth and Planetary Science Letters*, **391**, 24–35, doi: [10.1016/j.epsl.2014.01.025](https://doi.org/10.1016/j.epsl.2014.01.025).
- Zhu, T. F., and K. Y. Chun, 1994, Understanding finite-frequency wave phenomena — Phase-ray formulation and inhomogeneity scattering: *Geophysical Journal International*, **119**, 78–90, doi: [10.1111/j.1365-246X.1994.tb00914.x](https://doi.org/10.1111/j.1365-246X.1994.tb00914.x).
- Zhu, Y., and I. Tsvankin, 2006, Plane-wave propagation in attenuative transversely isotropic media: *Geophysics*, **71**, no. 2, T17–T30, doi: [10.1190/1.2187792](https://doi.org/10.1190/1.2187792).
- Zhu, Y., and I. Tsvankin, 2007, Plane-wave attenuation anisotropy in orthorhombic media: *Geophysics*, **72**, no. 1, D9–D19, doi: [10.1190/1.2387137](https://doi.org/10.1190/1.2387137).